Automation in Construction 150 (2023) 104811

Contents lists available at ScienceDirect

Automation in Construction

journal homepage: www.elsevier.com/locate/autcon

Measuring annular thickness of backfill grouting behind shield tunnel lining based on GPR monitoring and data mining

Li Zeng [a,b,d], Xiaobing Zhang [c], Xiongyao Xie [a,b,*], Biao Zhou [a,b], Chen Xu [a,b], Sébastien Lambot [d]

[a] Department of Geotechnical Engineering, College of Civil Engineering, Tongji University, Shanghai 200092, PR China
[b] Key Laboratory of Geotechnical & Underground Engineering of Ministry of Education, Tongji University, Shanghai 200092, PR China
[c] Tianjin Underground Railway Group Co., Ltd, Tianjin 300000, PR China
[d] Earth and Life Institute, Université catholique de Louvain, Louvain-la-Neuve 1348, Belgium

ARTICLE INFO

Keywords:
Metro shield tunnel
Ground penetrating radar
Backfill grouting
Automation
Non-destructive testing (NDT)
Extreme gradient boosting (XGBoost)

ABSTRACT

Ground-Penetrating Radar (GPR) has been widely used in the backfill grouting detections of shield tunnel construction. The proposed approach of automatic annular thickness measurement based on GPR monitoring system and BBP-XGBoost algorithm has been demonstrated to be an effective and efficient technique for detecting the backfill grouting of shield tunnel construction. The advantages include: (1) high accuracy: the proposed model is able to achieve high coefficients of regression R2 (0.943) for training sets and comparatively low RMSE values (0.421 and 1.32 cm) for both training and testing datasets, respectively; (2) high efficiency: the proposed XGBoost algorithm outscores other models in both accuracy and efficiency; (3) real-time output: the trained models were applied to automatically measure the annular grouting thickness of the Tianjin Metro tunnel constructions (China), with consistent real-time outputs for the engineers on site. The proposed approach provides real-time and efficient guidance for the construction of shield tunnels.

1. Introduction

Grouting is a common practice for filling the gap between the tail shield of a tunnel boring machine and the tunnel concrete lining during the construction of shield tunnels, especially in densely-populated urban areas. The uniform-distributed grouting layer behind the linings serves as the primary method to control ground settlement and the first waterproof front of the tunnel structures. This layer of grouting can effectively reduce the ground settlements and the erosions of the tunnel lining by groundwater, and significantly reduce the leakage of the tunnels [1]. However, if this layer is insufficient or unevenly-distributed, it can cause uneven ground settlements and water leakage at the joints of tunnels, which can compromise the safety of tunnel construction and operations [2].

Emerging non-destructive testing (NDT) technologies offer new approaches and capacities to monitor the grouting during both constructions and operations. Given its fast featuring and high-resolutions, ground penetrating radar (GPR) technology, as one of the most important and effective non-destructive tools, has been increasingly used in tunnel structure inspections [3,4]. The backfill grouting is constructed within a range of approximate 1 m behind the tunnel linings, where concrete linings, backfill grout, and soils can be detected by the GPR. [5] A novel real-time back-fill grouting monitoring system and tunnel inspection vehicle has been developed, which is based on the integration of a new GPR monitoring system in a shield tunnel machine [6]. Since GPR waveform data does not directly provide information regarding the distributions of the subsurface media, the interpretation of GPR data for buried structures has become a subject of wide academic interest and research. [7]. In tunnel construction sites, processing GPR radargrams to identify buried underground structures has always been a problem that plagued the application of GPR monitoring technology. Substantial effort has been invested in interpreting the GPR radargrams to seek different targets and pertinent potential structural diseases [8–13]. Zhai et al. introduced an imaging algorithm to enhance the radar reflections waveform based on the bi-frequency GPR antenna [10]. The interpretation of subsurface structures using GPR radargrams requires advanced technical expertise on the part of the engineer. Qin et al. [11] managed to develop a series of algorithms and to calculate the thicknesses of grouting through numerical experiments, yet more on-site validations needed to be resorted. Zhao et al. [14] introduced the multiple suppression algorithm for processing the GPR data concerning backfill grouting, with enhanced reflections observed in the processed GPR data.

* Corresponding author at: School of Civil Engineering, Tongji University, Shanghai 200092, China.
E-mail address: xiexiongyao@tongji.edu.cn (X. Xie).

https://doi.org/10.1016/j.autcon.2023.104811
Received 31 August 2022; Received in revised form 14 February 2023; Accepted 21 February 2023

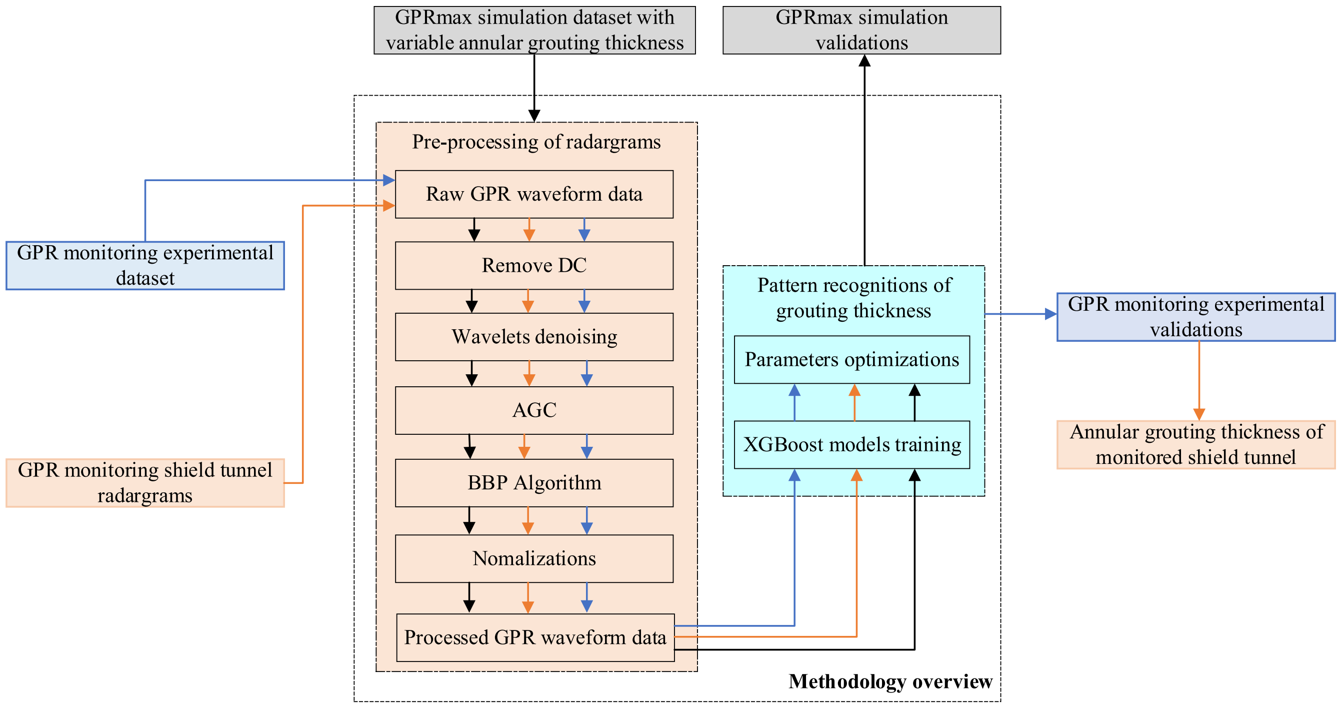

Fig. 1. Flows of methodology overview.

Xie et al. [15] recommended algorithms (band-pass and K-L filter) for GPR data processing concerning existing backfill grouting. The application of these methods has improved the GPR data features, especially in the deeper regions, where the weak waveform reflections have become more discernible, thereby providing engineers with more recognizable images. However, the results should still be thoroughly interpreted by experts who possess vast knowledge and expertise in GPR and tunnel engineering.

Recent years have seen a proliferation of research into the application of machine learning (ML) techniques to the analysis of structural monitoring data [13,16,17]. Qin et al. [18] used deep convolutional networks with data augmentation to estimate the thicknesses and probable voids in the mountainous tunnel linings from the GPR data. Liu et al. [19] set up a deep learning network to analyze GPR data for localizing the reinforcements in the concrete structures. Yue et al. [20] carried out a generation of GPR images using improved least squares GAN for detecting rebars. Akçali S [21] studied a region-based convolutional neural network (RCNN) algorithm adapted for the buried target detections. Faster-RCNN frameworks were used by Minh-Tan Pham [22] for searching the hyperbola characters in the GPR data images. The ML methods were also adopted by Lameri [23] for the landmine recognition based on GPR and convolutional neural networks. Yamaguchi [24] explored the 3-D convolutional neural network and Kirchhoff migration for pipe inspection. Feng et al. [25] conducted robotic inspection of underground utilities for construction survey based on learning-based migration module. Feng et al. [26] also improve the 3D GPR imaging by introducing a learning-based GPR data analysis method, which includes a noise removal module to clear the background noise in raw GPR data and a Convolutional Recurrent Neural Network (CRNN) to estimate the dielectric value of subsurface medium in each GPR B-scan data. **Based on the literature review, machine learning (ML) techniques have been applied to numerous Ground Penetrating Radar (GPR) applications, such as pipes, rebars, and concrete targets, for data interpretation. However, the performance of ML techniques in estimating the annular thickness of backfill grouting is yet to be explored. GPR data related to the monitoring of backfill grouting lack clear waveform features, making it more challenging to interpret than the other GPR-ML practices previously reported in literature.**

This paper proposes an annular grouting thickness monitoring method based on GPR monitoring system and novel extreme gradient boosting approach (XGBoost) algorithm [27,28]. The proposed method improves the efficiency of interpreting GPR data for annular grouting thickness in tunnels. The paper is structured as follows. Section 2 presents an overview of the proposed method, including the preprocessing steps and a brief introduction of the principle of the Bi-frequency back projection-eXtreme Gradient Boosting (BBP-XGBoost) joint approach. Section 3 presents techniques for establishing the training GPR waveform data through gprMax numerical simulations [29], and demonstrates the correlation between the accuracy of the XGBoost model and the degree of noises in the GPR simulation dataset. Section 4 discusses the full-scale experimental tests designed to establish the real GPR waveform dataset and the GPR monitoring system application in Tianjin metro 6. Additionally, it discusses the algorithms' performances in predicting the annular grouting thickness of the Tianjin tunnels. Finally, Section 6 draws the conclusion that XGBoost showed the best performances in terms of accuracy on the GPR dataset and least time consumption. The proposed method and work introduced in this paper could provide real-time references for grouting constructions in shield tunneling, and could be applied to other GPR applications. Moreover, it could also inspire further studies in the field of GPR data interpretation with machine learning.

2. Overview of the methodology

The methodology overview of this paper is presented in Fig. 1. Preprocessing and Pattern Recognition Algorithm modules are developed for the GPR waveform datasets. Subsequently, gprMax simulation dataset and GPR monitoring experimental dataset are used to train and validate the algorithm modules. After training, the modules are adopted for predicting the annular grouting thickness based on GPR monitoring shield tunnel grouting radargrams.

2.1. Wavelet analysis and denoising theory

2.1.1. 1-D wavelet analysis

GPR waveform data is a type of time-space sequence data, which possesses non-linearity and high signal-to-noise ratio characteristics. Traditional methods such as Gaussian denoising and median filtering often have multiple drawbacks. Therefore, wavelet theory has been developed to meet the requirements of time-frequency localization. Wavelet transform has become increasingly valued and adopted for signal processing in an array of academic research, yielding impressive outcomes in a wide range of applications. It is a time-frequency domain positioning analysis method that uses a fixed window size but is capable of changing the shape of wavelets. Wavelets are linear, narrow-band filters that can be rescaled to longer or shorter lengths, providing a set of convolutional filters that can detect features with scales matching the filters' bandwidth. 1-D Wavelet Filters can also act as frequency filters with various localization properties (scale) [30].

Assuming that $WT(\alpha,\tau)$ is a wavelet transform result, whose inner product is a square integrable function then

$$WT(\alpha,\tau)=\frac{1}{\sqrt{\alpha}}\int_{-\infty}^{+\infty}f(t)^{*}\psi\left(\frac{t-\tau}{a}\right)dt \tag{2.1}$$

where, α and τ are the scaling factor and translation factor, respectively; $\psi(t)$ is the basic wavelet function; $f(t)$ is the original signal needed to be processed.

From a signal science standpoint, wavelet denoising is a signal filtering problem, which can largely be seen as a low-pass filter. Yet, wavelet denoising has the advantage of preserving signal characteristics after denoising, making it a more effective approach than traditional low-pass filtering. This is due to the combination of feature extraction and low-pass filtering that wavelet denoising employs.

In this paper, the PyWavelets [31] library provided by Python are adopted for wavelet analysis. PyWavelets provides a total of 14 wavelet basis functions, of which the ***db*** and ***sym*** wavelet system has good orthogonality and good sensitivity to non-stationary sequences, and it is proved in the literature that it is effective in denoising the monitoring sequence. [31].

2.1.2. Denoising based on wavelet transform analysis

For the selection of wavelet basic functions and decomposition layers, several patterns should be aware of. If decomposition layers are too less, the amount of information contained in each layer is relatively large, and the denoising process is likely to lose effective information, resulting in poor results. If decomposition layers are too many, the noise information will be distributed in more layers, making noise removal difficult. According to the literature found [32], the range of decomposition layer were determined between 2 and 6.

There are three main evaluation indexes of wavelet denoising effect [32], namely, smoothness index (r), signal-to-noise ratio (SNR), and root mean square error (RMSE).

For RMSE,

$$RMSE=\sqrt{\frac{1}{n}\sum_{i=1}^{n}\left[f(i)-\widehat{f}(i)\right]^{2}} \tag{2.2}$$

where, $f(i)$ is the original signal; $\widehat{f}(i)$ is the decomposed and reconstructed signal under a certain filter, and n represents the signal length, the same below.

For r,

$$r=\frac{\sum_{i=1}^{n-1}\left[\widehat{f}(i+1)-\widehat{f}(i)\right]^{2}}{\sum_{i=1}^{n-1}\left[f(i+1)-f(i)\right]^{2}} \tag{2.3}$$

For SNR,

$$\mathrm{snr}=-10lg\left(\frac{\sum_{i=1}^{n}p_{\widehat{f(i)}}}{\sum_{i=1}^{n}p_{f(i)}}\right) \tag{2.4}$$

where, $p_{\widehat{f(i)}}$ and $p_{f(i)}$ represent the power of certain signals, respectively, the same below.

It can be considered that the smaller the smoothness index, the smoother the signal and the better the denoising effect.

The root mean square error only describes the difference in the details of the denoised GPR signals, focusing on the detailed information of the signals; however, the smoothness (r) focuses on approaching GPR signals, and describes the overall trend characteristics of the denoising signal. Therefore, in order to examine whether the overall trend of the signal is well preserved after being denoised, the smoothness index must be used.

In this paper, comprehensive evaluation index concerning both RMSE and smoothness are adopted [31]:

$$E=W_{NRMSE}\times NRMSE+W_{Nr}\times Nr+W_{Nsnr}\times Nsnr \tag{2.5}$$

where, W is the weight calculated based on the coefficient of variation. $NRMSE$, Nr and$Nsnr$are the normalization form of RMSE, r and snr, respectively. According to the above monotonicity of the root mean square error and smoothness, it can be seen that the smaller the E value, the better the denoising effect. Given that the comprehensive metric can merely evaluate one trace of the GPR radargrams, the mean of all GPR traces for calculating the E values and choosing the wavelets basic functions and decomposition layers are adopted:

$$Mean_{Ascan}=\frac{1}{k}\sum_{i=1}^{k}Ascan_{i} \tag{2.6}$$

where A-scan is the single-channel trace of GPR the radargrams.

2.2. Bi-frequency back projection method

The Bi-Frequency Back-Projection (BBP) Algorithm was utilized to attain a high-quality visualization of the grouting distribution [10]. BBP is designed to enhance the detection quality and is based on the simultaneous use of two B-scans of distinct dominant frequencies, 400 MHz and 900 MHz, which were adopted in the Ground Penetrating Radar (GPR) monitoring system applied in this experiment and site application. In this paper, the BBP method was employed for pre-processing and dual-frequency imaging for further machine learning.

2.3. Ensemble learning and extreme gradient boosting tree (XGBoost)

The decision tree enhancement is an efficient and widely used machine learning method. In this paper, a scalable end-to-end tree augmentation system called XGBoost were resorted, which has been widely used by data scientists to obtain the latest results in many machine learning challenges [27]. For the GPR radargrams being processed by the preprocessing steps, it still needs professional advices to identify the grouting. The adoption of the XGBoost aims at learning the relationships between the patterns of the radargrams and the thickness of the grouting.

As an efficient implementation of GBDT, XGBoost is an algorithm with a particularly high upper limit, so it is more popular in algorithm competitions. Simply put, compared to the original algorithm GBDT (Gradient Boosting Decision Trees) [28], XGBoost is mainly optimized from the following aspects.

First, the optimization of the algorithm itself: in the selection of the algorithm weak learner model, compared to GBDT only supporting decision trees, many other weak learners can be directly used. Second, in the loss function of the algorithm, in addition to its own loss, a

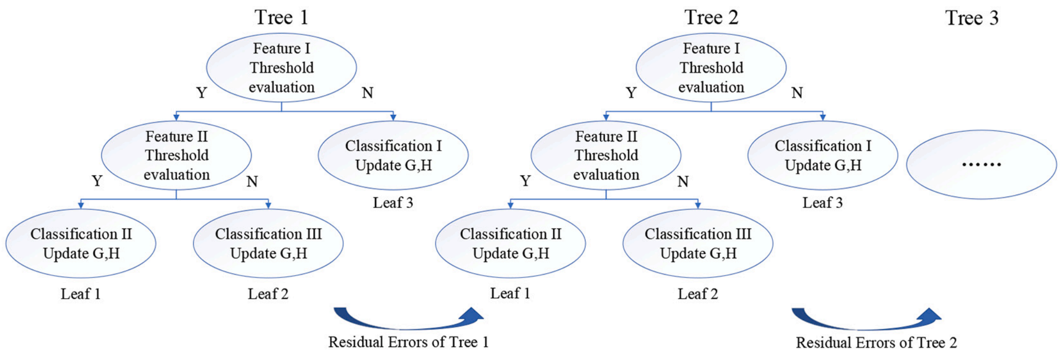

Fig. 2. Schematic of XGBoost Trees and the transmissions of residual errors.

regularization part is also added. In the optimization method of the algorithm, the loss function of GBDT only performs a negative gradient (first-order Taylor) expansion on the error part, while the XGBoost loss function performs a second-order Taylor expansion on the error part, which is more accurate.

The main flow of the XGBoost algorithm is hereby summarized, which is based on the decision tree weak classifier.

The input is a GPR waveform training set sample $I = \{(x_1,y_1),(x_2,y_2),(x_3,y_3),\dots(x_m,y_m)\}$, where x_i represents processed GPR waveform and y_i represents the annular thickness of grouting. The maximum number of iterations is T, the loss function L, the regularization coefficients are λ, γ.

The output is a strong learner $f(x)$.

For the number of iterations $t = 1, 2, \dots T$,

(1) Calculate the loss function L of the i-th sample (i-1,2,..m) in the current round based on the first derivative g_{ti}, second derivative h_{ti}, and then calculate the sum of the first and second derivatives of all samples $G_t = \sum_{i=1}^{m} g_{ti}$ and $H_t = \sum_{i=1}^{m} h_{ti}$.

(2) Based on the current node trying to split the decision tree, the default score is 0. G and H are the sum of the first and second derivatives of the node that needs to be split.

For numbers of features $k = 1, 2, \dots, K$:

$$G_t = 0, H_t = 0$$

a) Arrange the samples according to the feature k from small to large, take the i-th sample in turn, and calculate the current sample in turn after classifying it into the left subtree, the sum of the first and second derivatives of the left and right subtrees:

$$G_L = G_L + g_{ti}, G_R = G - G_L$$

$$H_L = H_L + h_{ti}, H_R = H - H_L$$

Try to update the maximum score:

$$score = max\left(score, \frac{1}{2}\frac{{G_L}^2}{H_L+\lambda} + \frac{1}{2}\frac{{G_R}^2}{H_R+\lambda} - \frac{1}{2}\frac{(G_L+G_R)^2}{H_L+H_R+\lambda} - \gamma\right) \tag{2.7}$$

(1) Split the subtree based on the divided feature and feature values corresponding to the maximum score.

(2) If the maximum score is 0, the current decision tree is established and then calculate ω_{ij} of all leaf areas. Therefore, the weak learner $h_t(x)$ is presented, update the strong learner $f_t(x)$ and then initial the next round of weak learner iteration. If the maximum score is not 0, go to step 2) and continue to split the decision tree.

The schematic of XGBoost Trees and the transmissions of residual errors are shown below in Fig. 2.

Table 1
The parameters involved in the gprMax numerical modeling.

Layers	Materials	Dielectric Constant	Thickness of materials (m)	Conductivity (mS/m)
Layer1	Air	1	0.1	0
Layer2	Concrete	6.5	0.35	0.1
	Reinforcements	∞	8Φ10 @ 0.2	∞
Layer3	Grouting	25	~N(0.13, 0.6)	5
Layer4	Soils	40	~N(1.37, 0.6)	15

3. Simulation and analysis

In Section 3, GPR simulations were conducted to validate the feasibility of the proposed idea. Section 3.1 outlines the details of the numerical modeling, Section 3.2 presents the results and analysis, and Section 3.3 provides an analysis of the anti-noise validation. The primary objectives of the GPR simulations were to conduct preliminary validations and analyze anti-noise effects.

3.1. Numerical modeling

3.1.1. gprMax 3.0 modeling

The numerical model was established using gprMax 3.0 [29] and Python programming environment, which is an open-source simulator solving the 3D Maxwell's equations using the Finite-Difference Time-Domain(FDTD)method [33]. The perfectly matched layer (PML) was implemented to avoid reflections from boundaries of the modeling domain [34]. It requires only a small number of mathematically-constructed cells for appropriate attenuation of reflections from the boundaries. In this case, the conductivity of PML regions was set as high as possible to achieve the complete absorption of propagating and evanescent waves thus eliminating electromagnetic boundary effects. Sources and receivers of antennas move along the air-segment interface (z = 1.9 m) every 0.005 m from x = 0.15 m to x = 0.85 m. The source pulse in the simulation is a Ricker wave with dominant frequencies of 400 MHz and 900 MHz, respectively, which is the same as what was adopted in the GPR monitoring system [6,10]. According to the frequency, the grid of the model is set to $dx = dz = 0.05$ m and $dy = 0.005$ m to ensure that the cells are smaller than one tenth the wavelength in the medium (condition to respect to minimize discretization effects). Since the maximum possible time step determined by Eq. (2.6) is 0.0024 ns, the time step dt is set to 0.002 ns. Indeed, the time step dt should be:

$$dt \leqslant \frac{1}{c\sqrt{\frac{1}{(dx)^2}+\frac{1}{(dy)^2}+\frac{1}{(dz)^2}}} \tag{2.6}$$

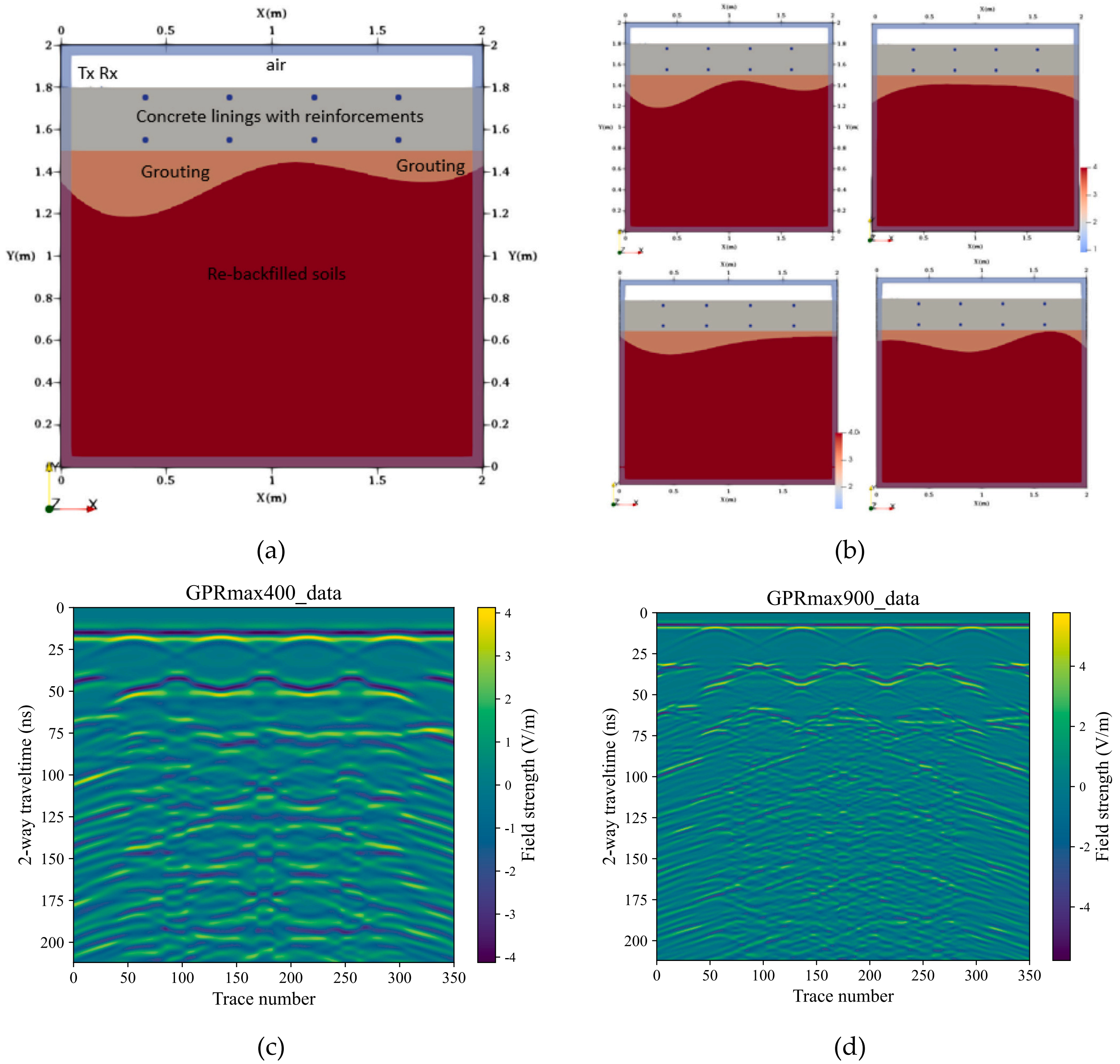

Fig. 3. The numerical modeling and bi-frequency dataset. (a) The layered media of numerical model. (b) The numerical models with variable annular thickness of grouting. (c) The raw numerical radargram of 400 MHz antenna. (d) The raw numerical radargram of the 900 MHz antenna.

3.1.2. The GPR waveform dataset of simulating the backfill grouting

Numerical modeling was used to evaluate the performance of an algorithm. Simulations of Tianjin metro line 6 on gprMax3.0 were conducted with the same size and electrical properties of linings, reinforcements, grouting, and soils as presented in Table 1. The thickness of the grouting was designed to simulate unevenly distributed grouting, as shown in Fig. 3, following a Gaussian distribution ~N (0.13, 0.06), which was based on the width of the theoretical gaps in the Tianjin tunnel construction. Thirty groups of models were simulated on gprMax3.0 using dual frequencies of 400 and 900 MHz. The resulting bi-frequency waveform datasets, consisting of more than 100,000 data points, were sufficient to test the XGBoost algorithm.

Table 1 summarizes the parameters adopted in the gprMax modeling. These parameters are based on the on-site experiment described in Section 4.1.2. The variable parameters include the thicknesses of grouting and corresponding soils, which have Gaussian distributions. This paper mainly adopts the XGBoost model, a predictive modeling technique that studies the relationship between GPR data and the spatially corresponding annular thickness of grouting.

3.1.3. Pre-processing in the numerical modeling of gprMax3.0

Prior to the implementation of data processing methods, a sequence of preprocessing steps must be completed, as illustrated in Fig. 4. Based on the literature, the following filters are used in sequence: DC component removal (DC is removed through average background subtraction), wavelet denoising, automatic gain control (AGC) according to the depths, and normalization. The purpose of DC component removal is to eliminate direct transmissions and reflections of electromagnetic waves between the transmitting and receiving antennas, which are often significant in the recorded waveform [35]. The use of Automatic Gain

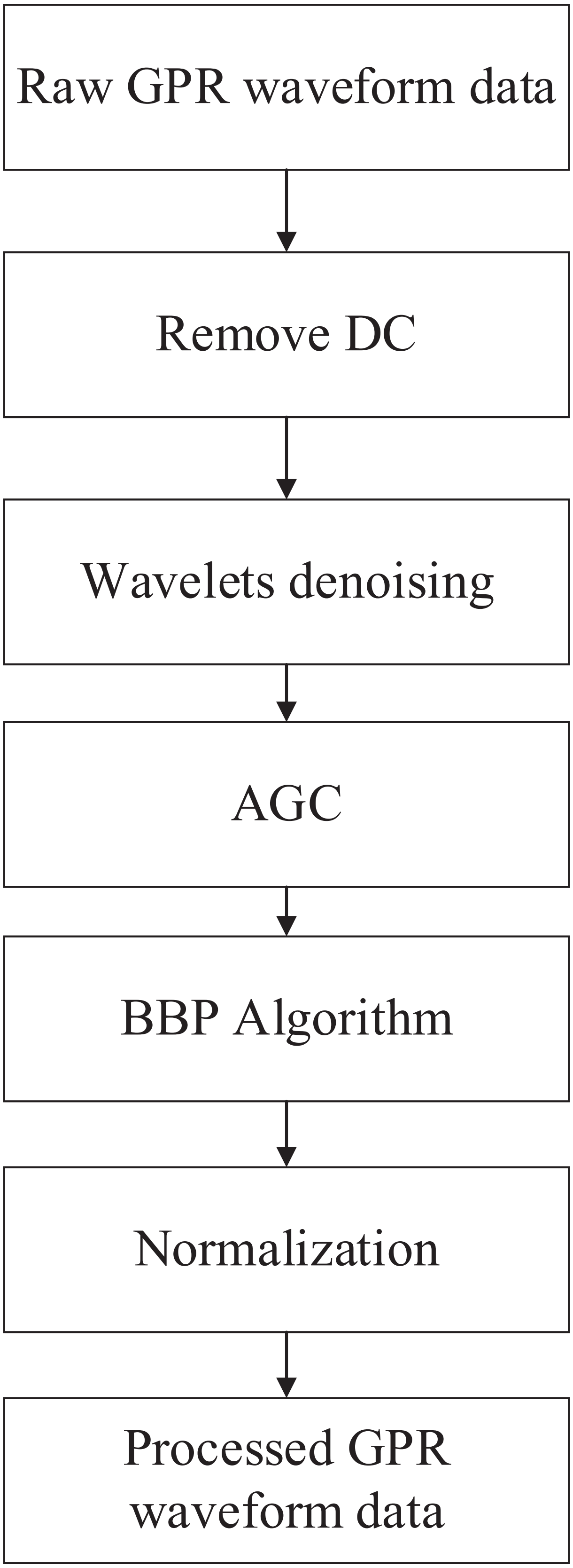

Fig. 4. The pre-processing algorithms adopted in the GPR data.

Control (AGC) in Ground Penetrating Radar (GPR) removes some of the near-field coupling between the antennas and the medium surface. This results in increased waveform strength in deeper regions, allowing for more reliable data acquisition [36]. The BBP algorithm was used to correlate and synthesize bi-frequency GPR data, resulting in the conversion of raw data into position-depth coordinates in both simulated and field test environments. Monitoring systems were used to record position-depth coordinates in the field tests [10]. Normalization was a common approach before machine learning algorithms were implemented, scaling the field strengths within −1 to 1.

3.2. Result and analysis

3.2.1. Wavelets evaluations of simulating GPR waveform data

Fig. 3(c) and (d) show the raw GPR radargram and the wavelets denoised radargrams, respectively. The mother wavelet function and decomposition layers were chosen based on the least evaluation metric. Fig. 5 indicates that *sym10* is a suitable mother wavelet function and three layers are an appropriate choice for decomposing the GPR data for denoising.

3.2.2. Simulating GPR waveform data after preprocessing

The preprocessing techniques employed were aimed at eliminating noise and enhancing the buried characters. The preprocessed gprMax simulated data are shown in Fig. 6. The data were examined and a dataset of more than 5000 preprocessed data with variable grouting thicknesses was established (see Fig. 3(b)).

3.2.3. The training XGBoost model for GPR numerical modeling data

The XGBoost algorithm, introduced by Chen and Guestrin, is a novel implementation of gradient boosting machines, specifically for regression trees [27]. This technique is based on the "boosting" concept, which combines the predictions of weak learners with additive training approaches to construct a powerful learner. Fig. 7 shows a decrease in RMSE and R2 scores as more weak learners (regression decision trees in this paper) are adopted in the boosting process, indicating the success of the XGBoost model training. As illustrated in Fig. 7, the RMSE metric reaches 0.022, close to 0, while $R^2 = 0.978$, close to 1, showing the model's convergence on the gprMax simulations dataset. The results indicate that the XGBoost model is capable of recognizing patterns and relationships between GPR datasets and grouting thickness. The simulation GPR dataset provides preliminary evidence for the feasibility of XGBoost training for the annular thickness of the grouting.

3.3. Anti-noises analysis

The goal of the gprMax modeling is evaluating the feasibility and accuracies of the XGBoost training on the GPR data. However, for the GPR monitoring system applied in tunneling environments, the GPR data collected are usually subjected to the noises and electromagnetic interferences. GPR data contaminated with different degrees of Gaussian noise as EM interferences are generated. The degrees of contaminations are also evaluated by Eq. (2.4). The results of the accuracies of XGBoost models are shown in Fig. 8. As the contaminations increase, the accuracies of XGBoost on test dataset has been inspected as a metric, however within tolerances from the perspective of engineers, gradually decrease. The definition of Accuracy of the test dataset is defined in Eq. (2.7).

$$\text{Accuracy} = \frac{Ture}{Ture + False} \tag{2.7}$$

Where *True* is the number of A-scan dataset in test dataset when the predictions of the grouting thickness equal to the ground truths, while *True* + *False* is the whole number of A-scan test dataset. The accuracy of the test dataset could reach **96%** when noises were not applied, which was the case in section 3.2.3. Gradual decrease of accuracy occurred as

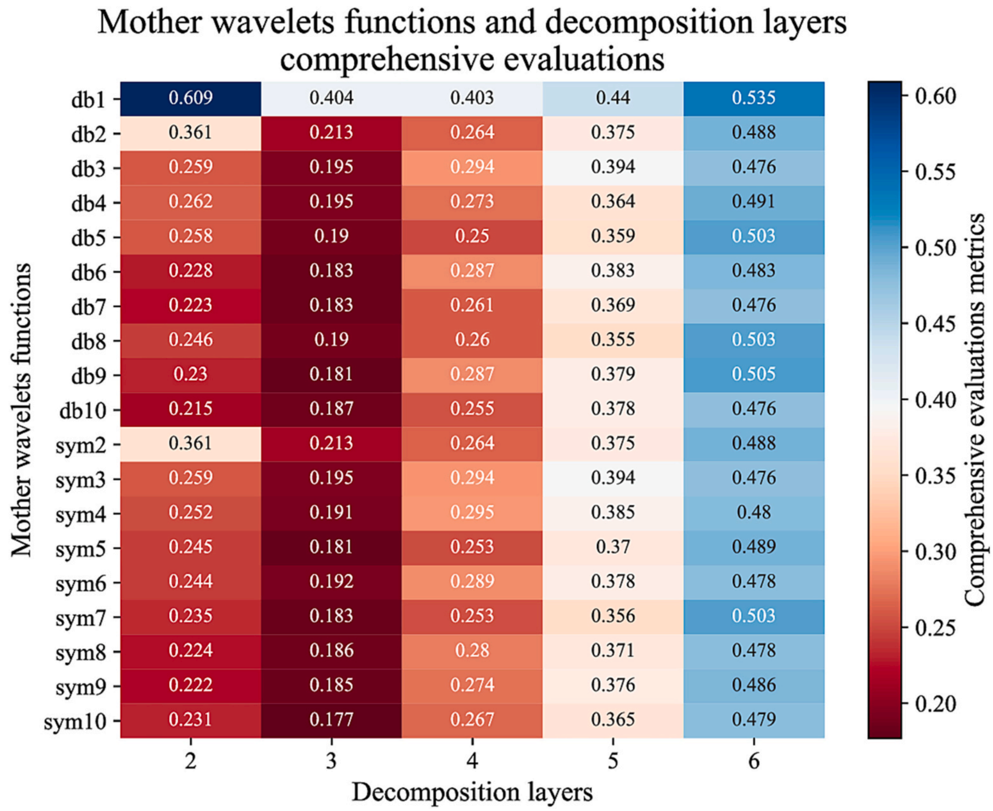

Fig. 5. Mother wavelets functions and decomposition layers comprehensive evaluations metrics for numerical experiments.

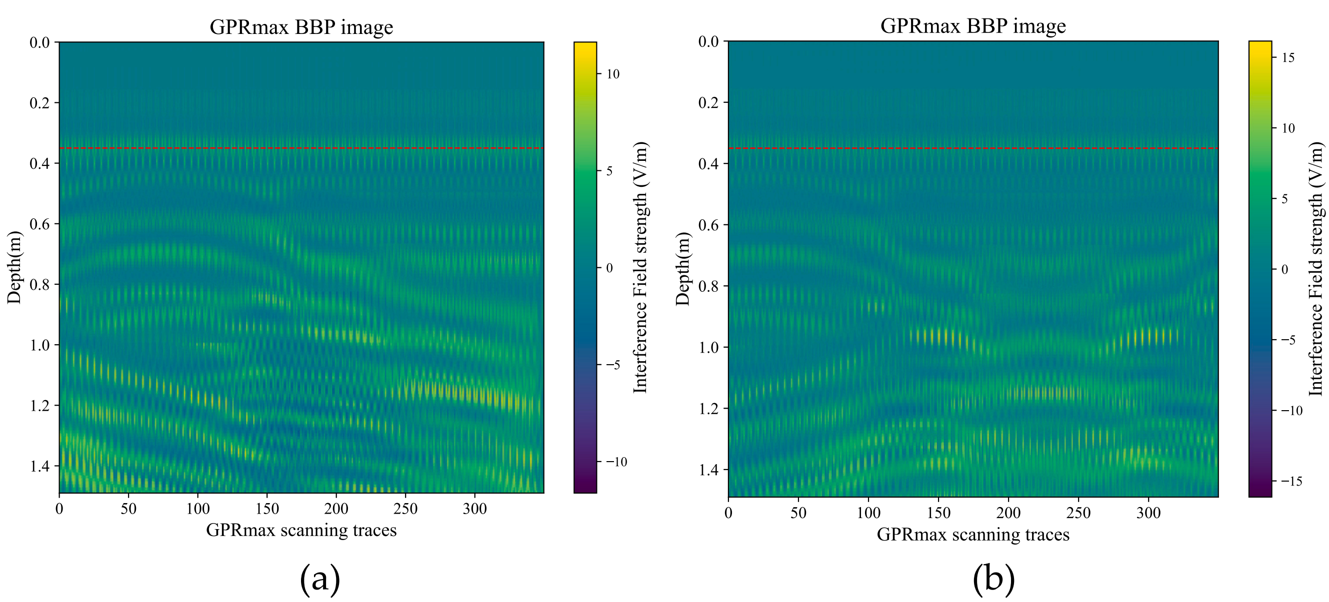

Fig. 6. The numerical modeling GPR datasets being preprocessed.

the dataset suffers more contaminations. More dataset of A-scans could show slightly fluctuations on accuracy, however, within tolerances from the perspective of tunnel engineering.

4. GPR monitoring full-scaled experiment and site application

In Section 4.1, a novel full-scale experiment involving a Ground Penetrating Radar (GPR) monitoring system and subway tunnels in Tianjin Metro Line 6 was conducted. This experiment provided a substantial amount of GPR waveform datasets for XGBoost algorithms. Section 4.2 outlines the engineering applications of this experiment, Section 4.3 provides an analysis of the algorithms and Section 4.4 presents the results.

4.1. GPR monitoring full-scaled experiment

4.1.1. The construction of the full-scale experimental site

An experimental setup was carried out in October 2020 at the Nankai

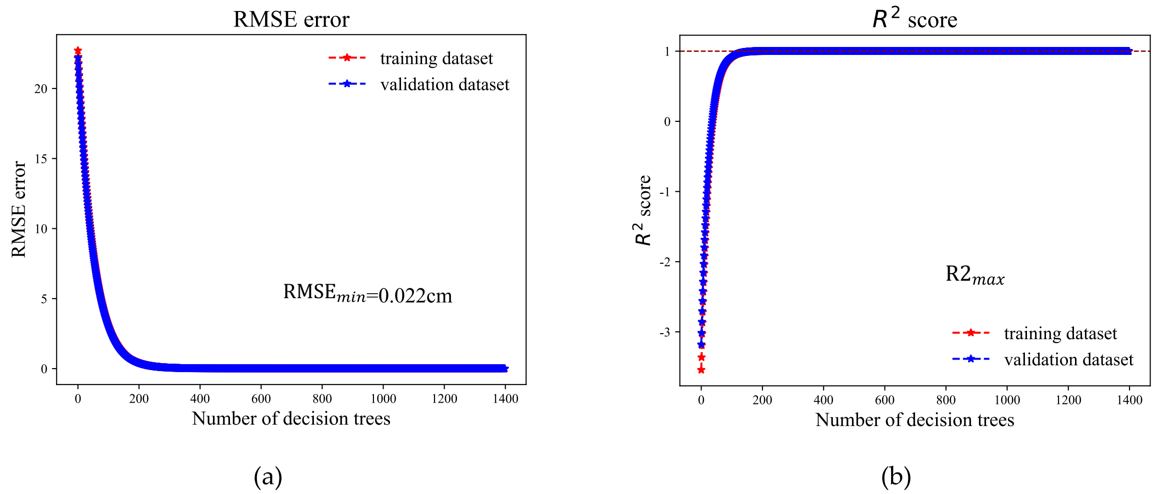

Fig. 7. The algorithm performances on the GPR data collected on the experimental tests. (a) The algorithm performances on numerical GPR data set with RMSE metric. (b) The algorithm performances on numerical GPR dataset with R^2 metric.

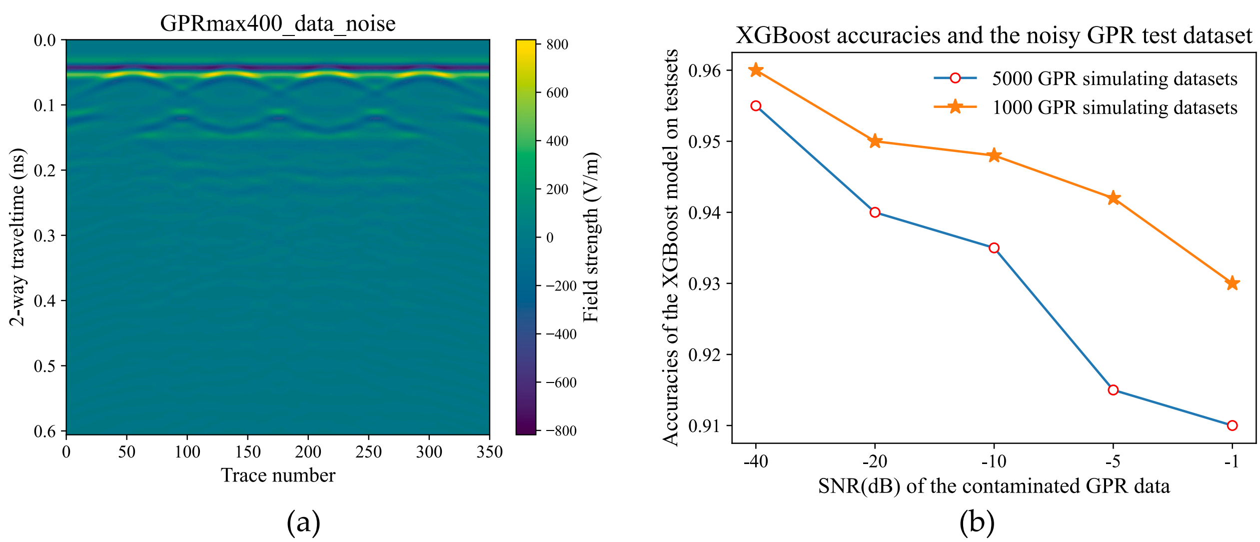

Fig. 8. The relation of algorithm performances and different degrees of noise in the GPR dataset. (a) The contaminated 400 MHz GPR dataset with the noises of -20 dB. (b) The relations of algorithm performances and variable noisy GPR dataset.

University Station of Tianjin Metro Line 6 to monitor the ground penetrating radar (GPR) performance. A full-scale model of the subway tunnel was built on a flat concrete platform, omitting the top segment of the shield tunnel lining. The tunnel linings were supplied by the construction company, with the same sizes and reinforcements as the ones used in the Tianjin metro line 6. The setup of the GPR monitoring experiments consisted of eight stages (Fig. 9):

(1) Construction of the plain concrete platform;
(2) Construction of the subway shield tunnel linings with the aid of crane machines;
(3) Installation of the GPR monitoring system, as shown in Fig. 9(a);
(4) Design of wooden formworks for shaping the grouting to variable annular thickness;
(5) Grouting construction (the grouting sully manufacturing company offered the same grouting used in subway construction), as shown in Fig. 9(b);
(6) Removal of wooden framework until grouting was mechanically self-sustaining;
(7) Earthwork re-backfills, as shown in Fig. 9(c);
(8) GPR monitoring tests, as shown in Fig. 9(d).

The results of the GPR monitoring experiments were then analyzed and used to evaluate the performance of the subway tunnel linings.

4.1.2. *Components and parameters of the full-scaled model*

In October–December 2020, a GPR monitoring system was applied to the Tianjin Metro Line 6 Nankai University Station experimental site. The shield tunnel lining had an inner diameter of 5900 mm, an outer diameter of 7100 mm, and a thickness of 350 mm. The ring width was 1.5 m and was composed of one capping block F (which was not adopted in the experiment), two adjacent blocks L, and three standard blocks B. All of these elements were tightly connected with 12 M30 ring bolts. The shield tunnel lining segments and their reinforcements are depicted in Fig. 10.

The GPR monitoring system employed in this experiment had been previously used for simultaneous grouting monitoring in numerous Chinese subway projects [6]. It was designed by Tongji University and manufactured by Dalian Zoroy Technology Development Co., Ltd. This system comprises two bowtie antennas with 400 and 900 MHz center frequencies, as adopted in the numerical experiments described in Section 3. The system permits the antenna to be driven along the track with a constant velocity, while simultaneously recording its positions and the

Fig. 9. The construction of the full-scaled experimental model. (a)The installation of GPR monitoring system. (b) Grouting construction. (e) The removal of wooden framework and the earthwork re-backfills. (f) The top view of GPR, tunnel linings, backfill grouting and soils.

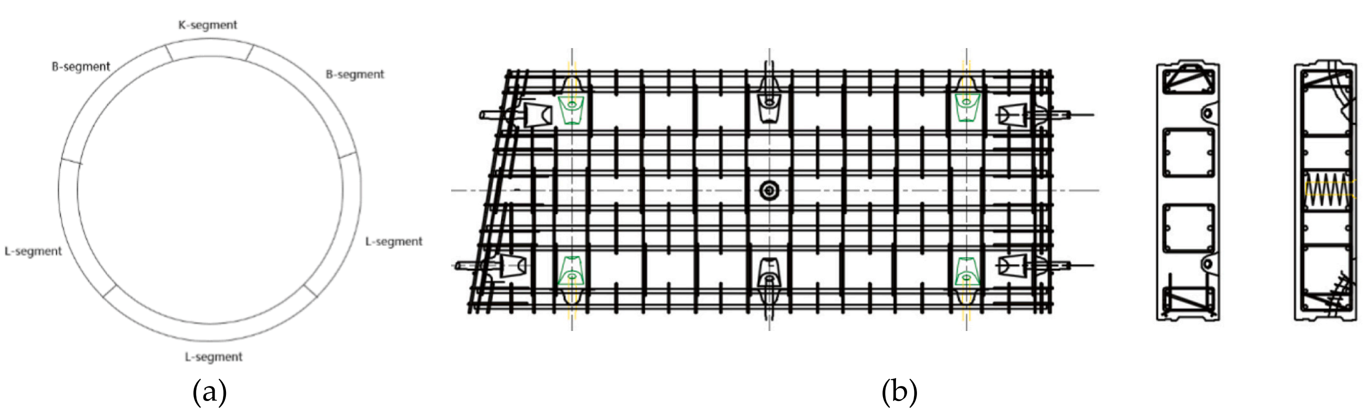

Fig. 10. The shield tunnel linings and the reinforcement in the full-scaled experiments. (a) The segments composed in the shield tunnel lining. (b) The reinforcements in the B-segment.

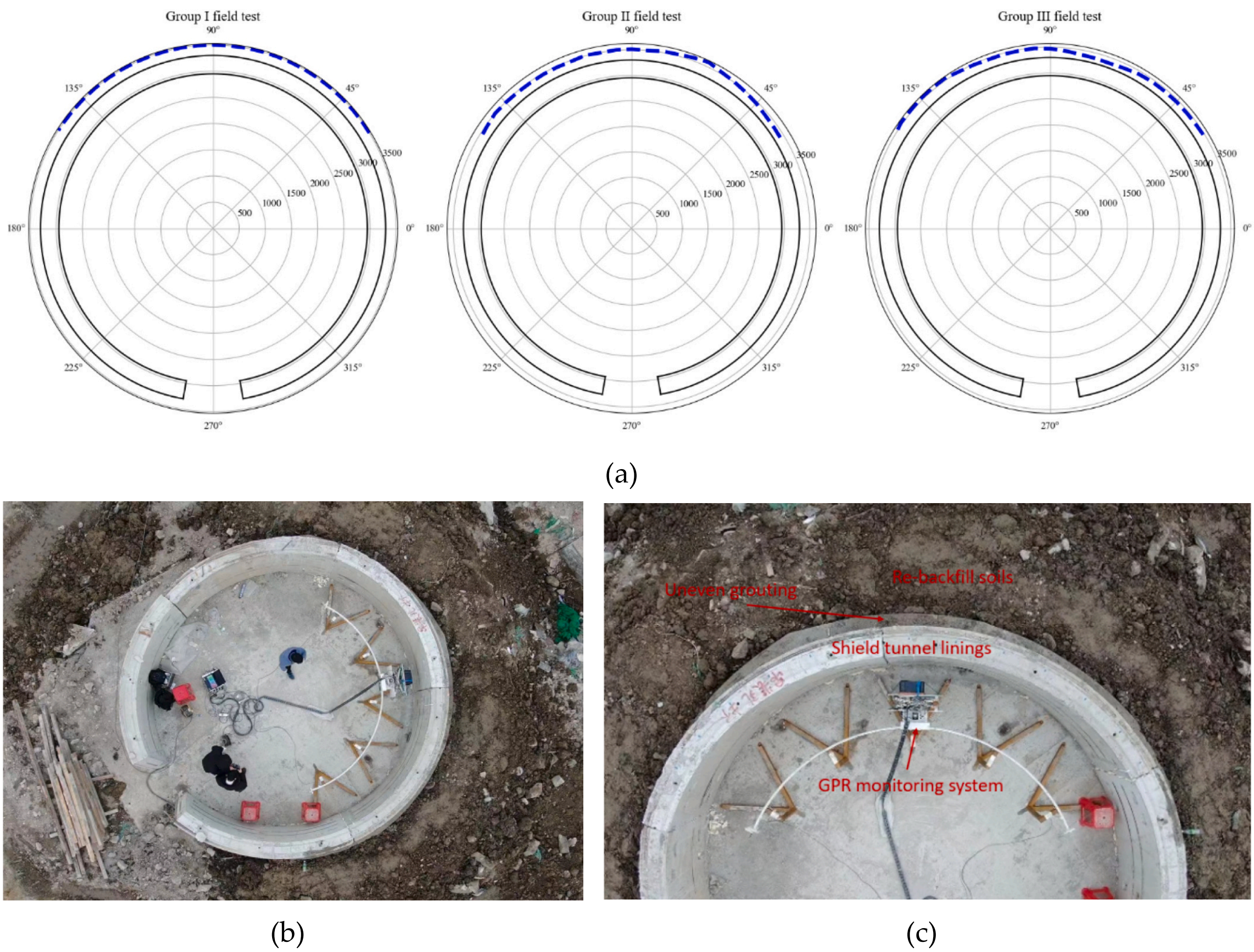

Fig. 11. GPR monitoring full-scaled test schemes. (a) The three group GPR field tests on unevenly-distributed grouting (blue dashes depicting the outlines of grouting shapes). (b) The aerial view of the experimental site during testing. (c) The aerial view of the soils, grouting, tunnel linings and GPR monitoring system. (For interpretation of the references to colour in this figure legend, the reader is referred to the web version of this article.)

Fig. 12. The dielectric constant and conductivity tests on (a) re-backfilled soils and (b) grouting materials.

Table 2
The ingredient proportions of grouting used in Tianjin subway and site experiment.

Materials	Volume	Cement (kg)	Fly ash (kg)	Sand (kg)	Bentonite (kg)	Water (kg)
Grouting	1 m^3	175	245	770	55	350

distance to tunnel linings through angle encoders. The track diameter was 5500 mm, and the distance of the antenna to the lining could be monitored and controlled using the distance encoders and the manufacturer software [6]. During the experiment, field GPR waveform data at distances of 100 mm, 150 mm and 200 mm were collected for each group of tests for subsequent mutual verifications. The monitoring process is illustrated in Fig. 11 (b) and (c). (See Fig. 12.)

The single-component grouting used in this experiment was provided by a manufacturing company that regularly supplies material for the Tianjin subway construction. The proportions of the grouting ingredients are listed in Table 2. In the construction of the Tianjin subway, four simultaneous backfill grouting machines are typically used for each ring, with two additional machines kept on standby for emergency use. Based on construction experience in Tianjin, the pressure of the grouting pipes of the shield machine is typically set at 5–6 bar. According to the shield machine and tunnel diameter designs, the theoretical gap is 3.80 m3, with an average annular gap thickness of 0.13 m. The grouting amount is typically designed to be 130%–250% of the theoretical building gap [36].

In this experiment, three sets of wooden formworks were used to shape and constrain the annular thickness of grouting, which was measured by tape measures to be variably designed from 80 mm to 320 mm, as shown in Fig. 11(a). The initial setting time of the mortar mixture was observed to be around 4 h, after which the formworks could be removed as the grouting had become self-sustaining. To avoid boundary effects, the annular range of grouting and re-backfilled soils was designed to be much greater than that of the GPR monitoring area. Consequently, in the subsequent data processing, the GPR waveform data whose documented positions were located near the boundaries were discarded.

The electrical properties of grouting and soils were assessed over time using a Time Domain Reflectometry (TDR) (Model AZS-100 Handheld Meter) [37]. Results showed that the dielectric constant of soils was approximately 40 while the grouting varied between 20 and 30 as the mechanical strength gradually formed, as illustrated in Fig. 13. Based on the research reported by Refs. [5, 10], it has been demonstrated that considerable fluctuations in the GPR radargrams are expected at the corresponding depths when the dielectric constants of two

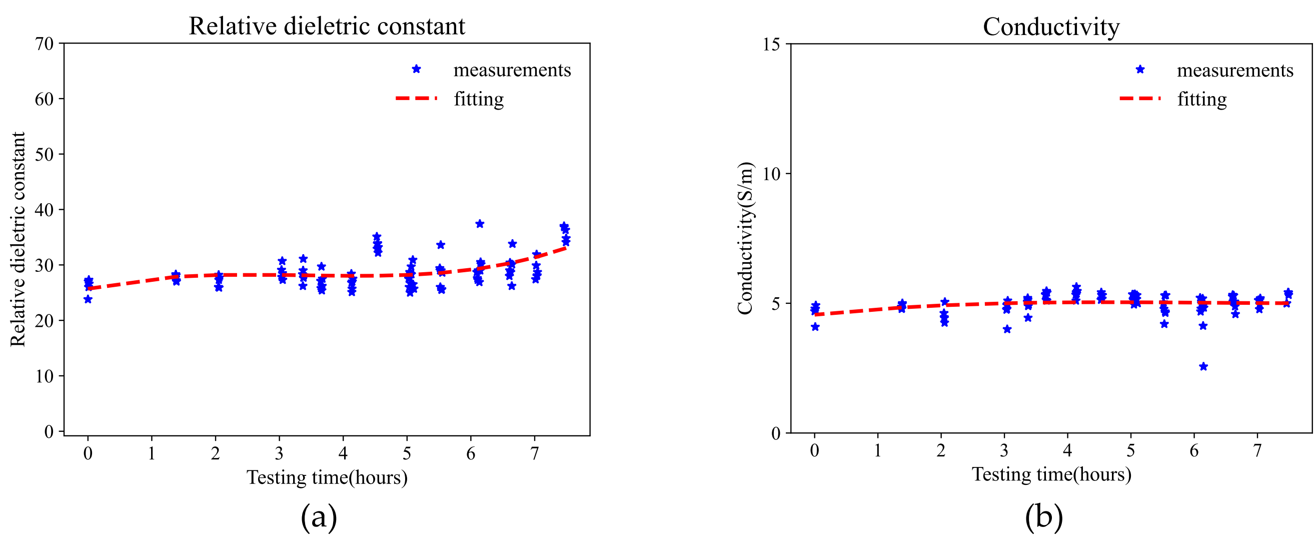

Fig. 13. The dielectric constant and conductivity measurements on the grouting in Tianjin: (a) relative dielectric constant and (b) electrical conductivity.

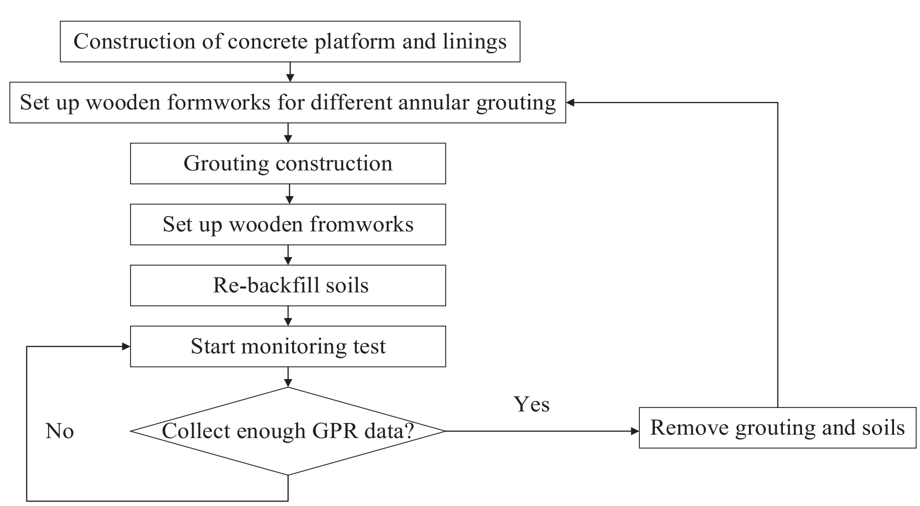

Fig. 14. GPR monitoring test workflow in full-scale experiment.

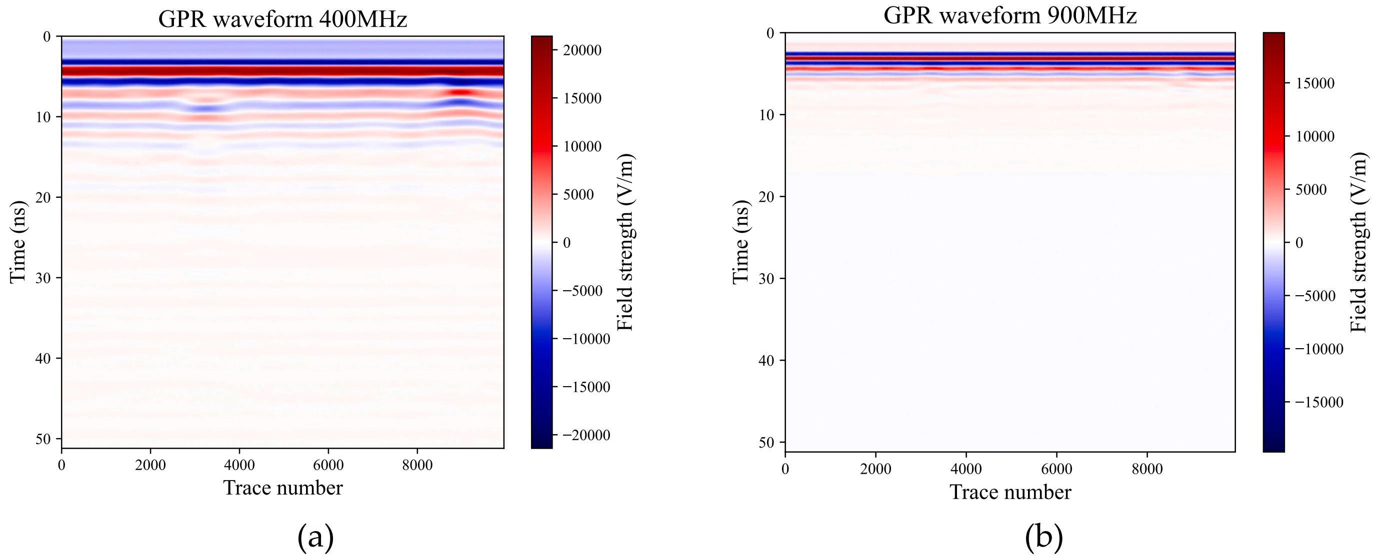

Fig. 15. Typical raw GPR radargrams on Field test I: (a) 400 MHz and (b) 900 MHz.

Table 3
The filters' parameters in the full-scale field tests.

Pre-processing Algorithms	Removing DC	wavelets denoising	AGC	BBP algorithm	normalization
Parameters	Remove the average of the GPR datasets	Mother wavelets: sym7 Decompositions:2 Denoising approach: hard-threshold denoising	AGC window: 5 ns	Dielectric permittivity: concrete 6.5 grouting 25 soils 40	Normalize to [−1,1]

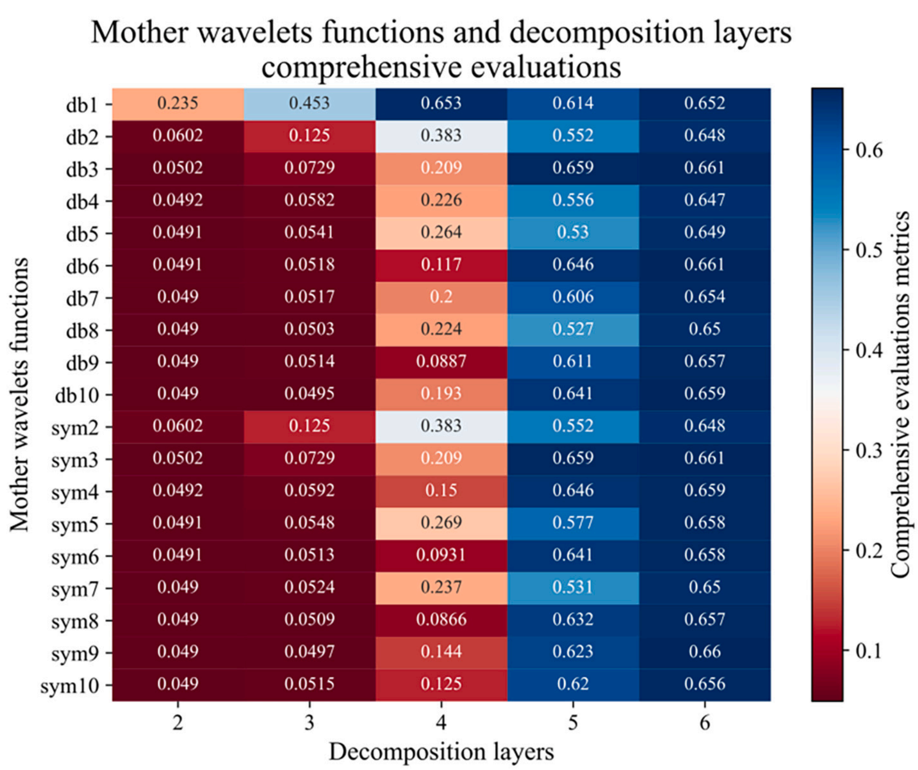

Fig. 16. Mother wavelets functions and decomposition layers comprehensive evaluations metrics for experiments on sites.

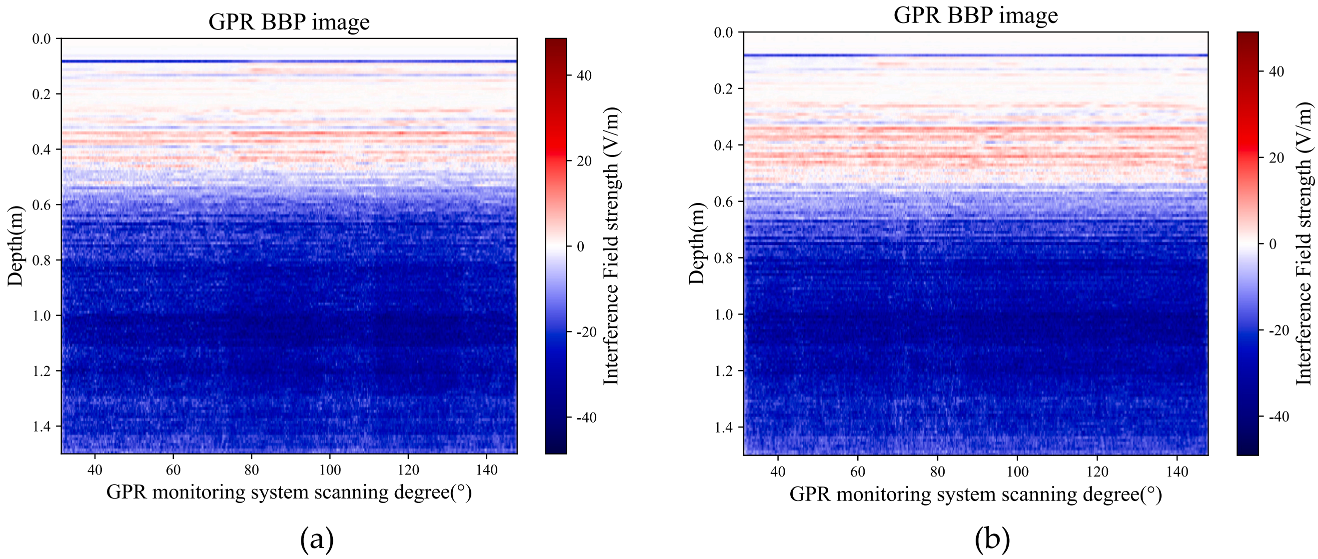

Fig. 17. The preprocessed radargrams of the field tests: (a) Field test II and (b) Field test III.

Table 4
The parameters involved in the training XGBoost models [27].

Training/validation/test set division ratio	Weak regressors	Learning rate	Trees Max depth	Regression labels	Number of early stopping rounds	The amount of GPR waveform data
8:1:1	CART regression trees	0.07	5	Thickness of grouting	100	10 GPR datasets from every 3 field tests Total 34,950 A-scans

adjacent materials differ considerably.

Fig. 13 shows that the dielectric constant and conductivity remain stable for a period of at least 7 h during parameter measurements. These results suggest that it is appropriate to set the grouting parameters at 25 for the dielectric constant and 5 mS/m for the conductivity.

4.1.3. Experimental workflow scheme

Upon completion of the concrete platform and linings, the wooden formworks were set up in accordance with the design of Group I test. Grouting was then injected into the gap between the linings and the formworks, after which the formworks were removed when the grouting was self-sustaining. Following this, the soils were re-backfilled and the monitoring test was initialized. Each test lasted 1–2 days, and during this time, 10–15 sets of GPR waveform data with more than 10,000 A-scans were collected. After the grouting and re-backfilled soils were removed via forklifts, another group of tests were initiated, following the same steps as outlined above. Fig. 14 illustrates the experimental workflow.

4.2. Experimental data and analysis

From the experiment, more than 10,000 GPR radargram data were collected and were processed by the preprocessing algorithms introduced in Section 2 with the sequence of Fig. 4. Fig. 15 shows the typical radargrams in the field tests.

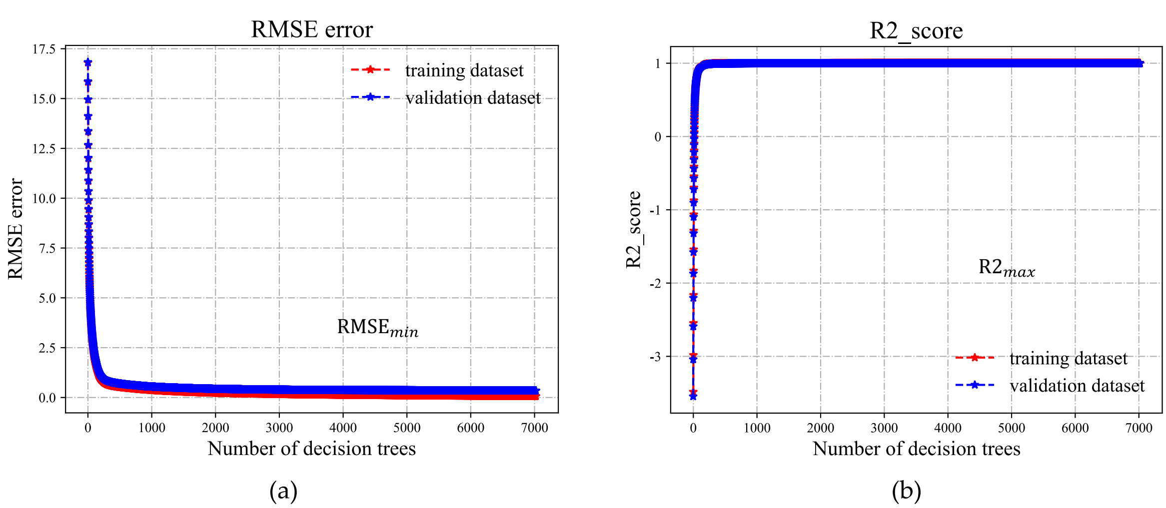

Fig. 18. The algorithm performances on the GPR data collected on the experimental tests. (a) The algorithm performances on data set with *RMSE* metric. (b) The algorithm performances on data set with R^2 metric.

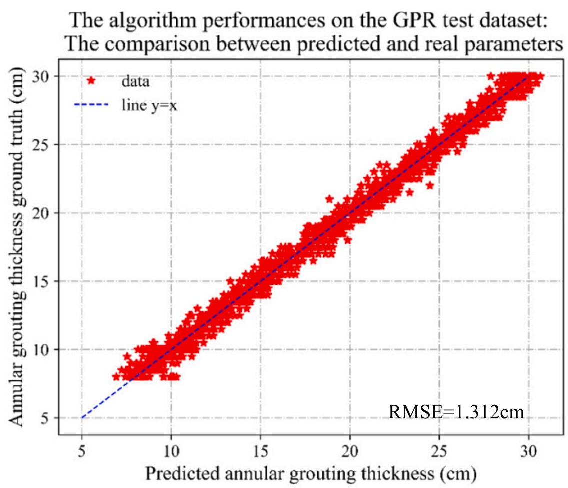

Fig. 19. The performances of algorithms on test GPR waveform datasets.

The data processing methods adopted in this part were the same as what was stated in the numerical experiments part. The filters' parameters in the field tests are shown in the Table 3.

The comprehensive evaluations of the basic wavelet functions and decomposition layers are presented in Fig. 16. Consequently, the mother wavelet function with the minimum comprehensive evaluation metric is chosen based on the evaluations indicated in the figure. The preprocessing methods applied to the radargrams allow for the visualization of the grouting layers to some extent. For the full-scale experiment case, the *sym7* mother wavelet function with 2 decomposition layers is deemed safe to use.

Fig. 17 illustrates the images obtained from the BBP algorithms. The images depict ambiguous layers, allowing engineers to recognize the concrete linings and grouts to a certain degree.

After preprocessing the data shown in the images into an appropriate dataset for training, validation, and testing, a machine learning training was conducted. Table 4 outlines the basic parameters and techniques used to train the XGBoost algorithms, including the implementation of an early-stopping technique to suppress over-fitting [27]. The results of the training and validation are depicted in Fig. 18. The training and validation process curves indicate that the models are well-converged.

As depicted in Fig. 18, the RMSE metric converges to 0.421 and the R^2 metric converges to 0.903, indicating that the XGBoost model exhibits good convergence on the full-scale experimental GPR datasets. The training process is similar to the one previously described in Fig. 7, only using the full-scale experimental GPR dataset. The full-scale experimental GPR dataset is initially fed into the XGBoost model, which is subsequently machine-learned, resulting in a model with good performance.

Fig. 19 illustrates the performance of machine learning algorithms on GPR test waveform datasets. The red dots represent predicted and real grouting thickness, while the blue line represents the line $\boldsymbol{y} = \boldsymbol{x}$. It is evident that the predicted and real grouting thickness values are fairly uniform and concentrated around the line $\boldsymbol{y} = \boldsymbol{x}$, indicating that the predicted and real grouting thicknesses are approximately equal within the given intervals. This analysis is essential when considering the feasibility and adaptability of the algorithms.

4.3. GPR monitoring system Tianjin metro line 6 site application

In December 2020, the GPR monitoring system was deployed from the experimental site and applied to the Tianjin Metro Line 6 Lushuidao station to the Shuanggang station section of the double single shield tunnel. This section had a circular double-hole single-track tunnel configuration, passing beneath Huanmei Apartment, Outer Ring Road and the Weishan Road Bridge. The parameters adopted for this tunnel were identical to those used in the experiment. During the tunnel construction, the GPR system monitored more than 300 rings of tunnel lining, collecting a considerable amount of data (as illustrated in Fig. 20). This application was similar to that of the GPR monitoring system deployed in the Jinan metro line in 2019 [6].

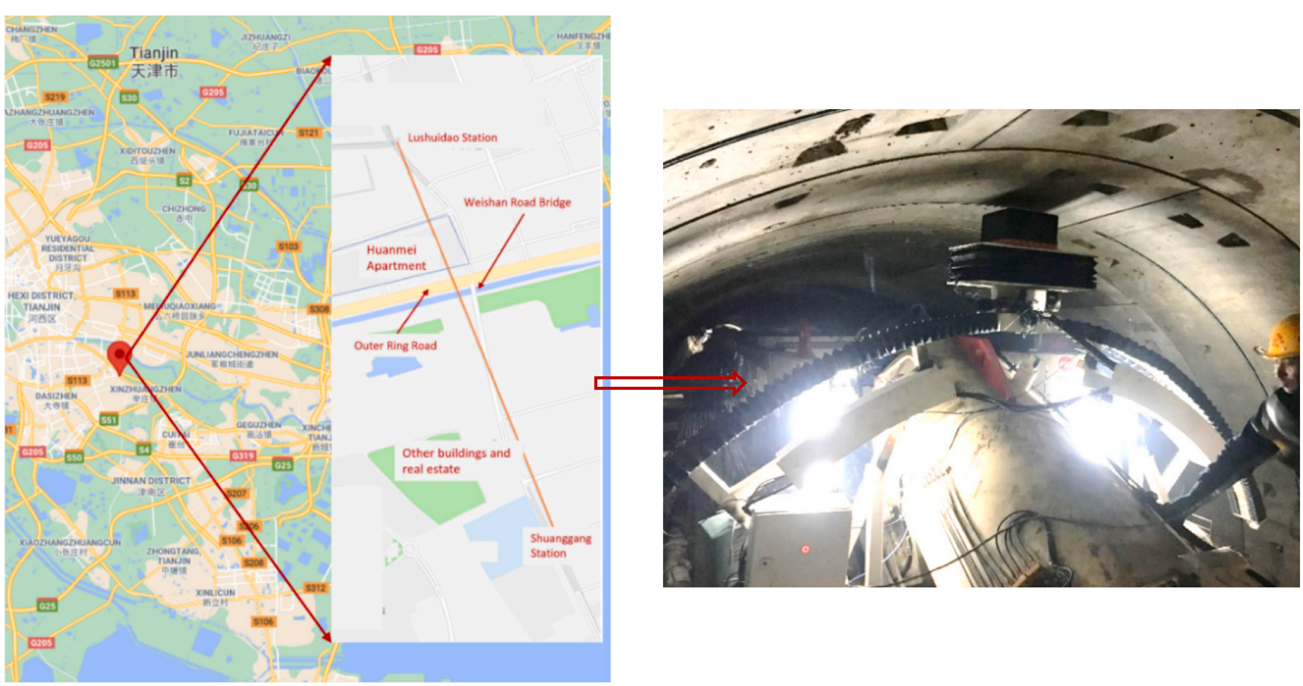

(a) (b)

Fig. 20. GPR monitoring system application in Tianjin Metro Line 6. (a) Location of Tianjin Metro Line 6 subway tunnel. (b) The application of GPR monitoring system in the tunnel.

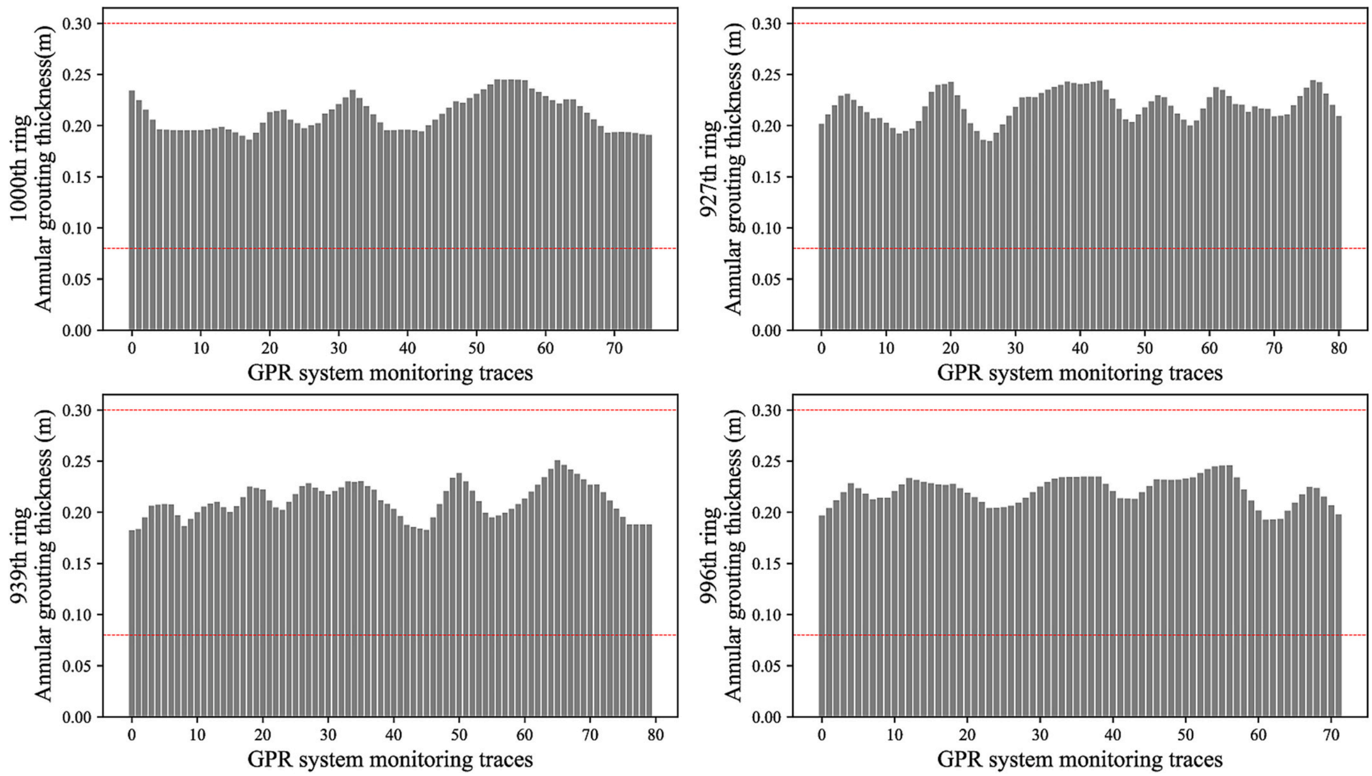

Fig. 21. The algorithm recognition of the annular grouting of subway tunnel in Tianjin Metro line 6.

Fig. 22. The automatic operation of GPR Monitoring System on tunnel construction site.

4.4. Algorithms application on sites

GPR data collected from experimental sites was used to train an XGBoost model, which was then saved as a file. This model can be used to predict the grouting layers during the construction of shield tunnels. Fig. 20(b) shows the GPR monitoring system that was used to monitor 200 rings of annular grouting. Fig. 21 displays the results of the XGBoost model applied to four selected rings. After preprocessing the data, the trained model can calculate the annular thickness for site engineers and technicians. The grouting of these four rings was mainly controlled between 150 mm and 250 mm, as observed from Fig. 21. The theoretical grouting thickness of Tianjin Metro line 6 shield tunnel was determined to be in the range of 100 mm to 300 mm [36]. The results of monitoring demonstrated that with the pretrained and preloaded model, the annular thickness of grouting could be automatically calculated and presented on the computer screens within 10 min. Furthermore, the recognition results could be easily accessed and referred to in the operation room with a few simple clicks on the software provided [6]. This enabled engineers to construct supplementary grouting in the case of uncompensated grouting after GPR monitoring, rather than after settlement, providing a much safer alternative in the densely populated urban cities of Tianjin. (See Fig. 22.)

5. Discussion

5.1. Algorithms application on sites

This study investigates the performances of various machine learning algorithms on a full-scale Ground Penetrating Radar (GPR) waveform dataset.

Analysis and comparisons of the performances of various machine learning algorithms on GPR waveform data have been conducted and the results are presented in Fig. 23. An artificial neural network (ANN) with a simple network structure and a deep neural network (DNN) were used to process the data, but their accuracies were underestimated and the training process took a considerable amount of time. In contrast, random forest consumed less time, but the accuracy was not satisfactory. The preprocessing time is also considered, as represented by the light blue columns in Fig. 23. XGBoost, however, required less training time and provided good accuracies, as illustrated in Fig. 23. The structures and hyper-parameters of the ANN and DNN used for comparison of the various ML methods are detailed in Table 5.

5.2. Limitations

The proposed BBP-XGBoost method integrated with the GPR monitoring system was demonstrated to effectively measure the annular grouting thickness in the range of 8 cm–30 cm in the Tianjin Metro Line project, where the soft soils have a low permeability coefficient and a single-component grouting was used. Further research is needed to

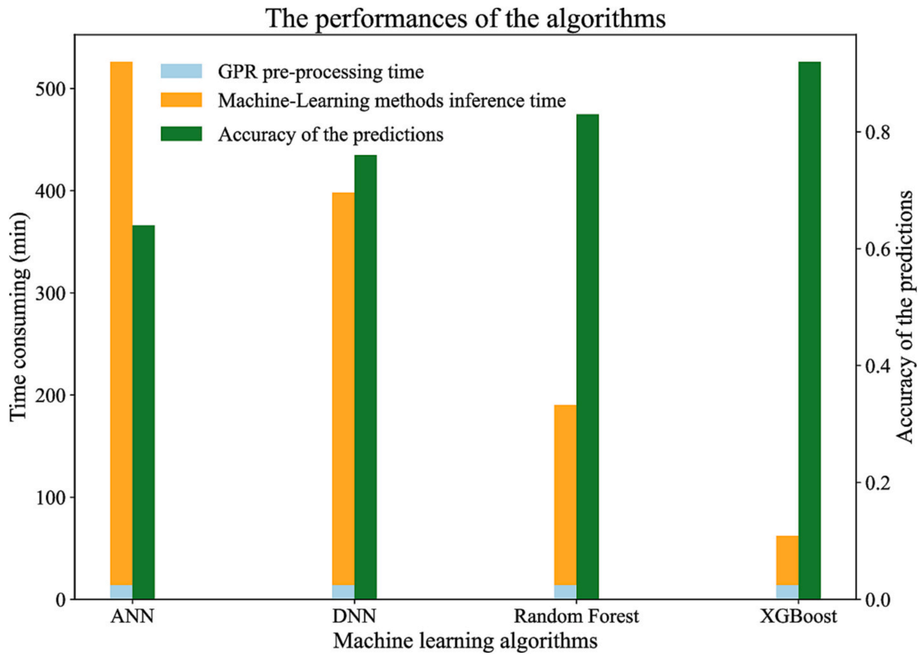

Fig. 23. The performances of different algorithms on GPR waveform dataset.

Table 5
The parameters involved in the training comparison models.

Algorithms	ANN	DNN	Random Forest
Structures	Input layers/ nodes:1/256 Hidden layer/ nodes:1/1024 Output layer/ nodes: 1/1164 (Output grouting thickness ranging from 8 to 30 cm)	Input layers/ nodes: 1/256 Hidden layer/ nodes:3/ 512–1024-512; Output layer/ nodes: 1/1164 (Output grouting thickness ranging from 8 to 30 cm)	Weak regressors: CART regression trees Trees Max depth: 5 Output: 1/1164 (Output grouting thickness ranging from 8 to 30 cm)
Hyperparameters	Optimization: Adam Dropout = 0.1 Learning rate = 0.1	Optimization: Adam Dropout = 0.1 Learning rate = 0.1	Number of early stopping rounds:100 Learning rate = 0.1

explore the performance of this method in other metro projects with different types of grouting materials and soils.

6. Conclusions

This paper presents a novel algorithm that utilizes an automatic predictive modeling technique to investigate the relationship between ground penetrating radar (GPR) data and the spatially corresponding annular thickness of grouting. Our findings show that the algorithm yields good results.

(1) A numerical FDTD modeling dataset is performed using gprMax for different thicknesses of annular grouting. After preprocessing, BBP-XGBoost model are trained and applied to the dataset. The accuracy on the test dataset reached 96%, indicating a successful result. Additionally, the anti-noise analysis indicated that the XGBoost model was able to maintain a satisfactory level of accuracy, even when subject to noises.

(2) The proposed BBP-XGBoost model was tested using a novel-designed experimental site at Tianjin Metro line 6, which collected a large amount of real GPR data. The results showed that the proposed model achieved satisfactory predictive performance, as evidenced by the high coefficient of regression R^2 (0.943) for the training sets and comparatively low RMSE values (0.421 and 1.32 cm) for both the training and testing datasets, respectively. Additionally, GPR data were acquired and used to train several algorithms for comparison. Of these algorithms, XGBoost demonstrated the best accuracies and lowest calculation time.

(3) Finally, the model was successfully applied to the tunnel construction in Tianjin Metro Line 6, providing real-time feedback for engineers onsite in terms of the thicknesses of annular grouting, thus reduce the labor intensity of the on-site engineers.

Author contributions

Li Zeng performed the methodology, formal analysis and wrote the manuscript; Xiaobing Zhang performed the project administration; Xiongyao Xie performed conceptualization and supervision; Biao Zhou performed the resources; Chen Xu performed the data curation; Sébastien Lambo performed the review & editing of the manuscript.

Funding

This research was funded by the National Key Research and Development Program of China under grant 2019YFC0605100 and 2019YFC0605103; the National Nature Science Foundations of China under grant 52038008; Shanghai Science and Technology Development Funds under grant 20DZ1202004, 22DZ1203004.

Declaration of Competing Interest

The authors declare no conflict of interest. The founding sponsors had no role in the design of the study; in the collection, analyses, or interpretation of data; in the writing of the manuscript, and in the decision to publish the results.

Data availability

No data was used for the research described in the article.

References

[1] X. Xie, Y. Yang, M. Ji, Analysis of ground surface settlement induced by the construction of a large-diameter shield-driven tunnel in Shanghai, China, Tunn. Undergr. Space Technol. (2016), https://doi.org/10.1016/j.tust.2015.10.008.

[2] Z. Huang, H. Fu, W. Chen, J. Zhang, H. Huang, Damage detection and quantitative analysis of shield tunnel structure, Autom. Constr. 94 (2018) 303–316, https://doi.org/10.1016/j.autcon.2018.07.006.

[3] A.P. Annan, 11. Ground-Penetrating Radar, in: Near-Surface Geophysics, Society of Exploration Geophysicists, 2005, pp. 357–438, https://doi.org/10.1190/1.9781560801719.ch11.

[4] W. Wai-Lok Lai, X. Dérobert, P. Annan, A review of ground penetrating radar application in civil engineering: a 30-year journey from locating and testing to imaging and diagnosis, NDT and E Int. 96 (2018) 58–78, https://doi.org/10.1016/j.ndteint.2017.04.002.

[5] F. Zhang, X. Xie, H. Huang, Application of ground penetrating radar in grouting evaluation for shield tunnel construction, Tunn. Undergr. Space Technol. 25 (2010) 99–107, https://doi.org/10.1016/j.tust.2009.09.006.

[6] L. Zeng, B. Zhou, X. Xie, Y. Zhao, H. Liu, Y. Zhang, I. Shahrour, A novel real-time monitoring system for the measurement of the annular grout thickness during simultaneous backfill grouting, Tunn. Undergr. Space Technol. 105 (2020), https://doi.org/10.1016/j.tust.2020.103567.

[7] S. Li, B. Liu, X. Xu, L. Nie, Z. Liu, J. Song, H. Sun, L. Chen, K. Fan, An overview of ahead geological prospecting in tunneling, Tunn. Undergr. Space Technol. (2017), https://doi.org/10.1016/j.tust.2016.12.011.

[8] X. Xie, H. Qin, C. Yu, L. Liu, An automatic recognition algorithm for GPR images of RC structure voids, J. Appl. Geophys. 99 (2013) 125–134, https://doi.org/10.1016/j.jappgeo.2013.02.016.

[9] H. Qin, X. Xie, J.A. Vrugt, K. Zeng, G. Hong, Underground structure defect detection and reconstruction using crosshole GPR and Bayesian waveform inversion, Autom. Constr. 68 (2016) 156–169, https://doi.org/10.1016/j.autcon.2016.03.011.

[10] X. Xie, J. Zhai, B. Zhou, Back-fill grouting quality evaluation of the shield tunnel using ground penetrating radar with bi-frequency back projection method, Autom. Constr. 121 (2021), 103435, https://doi.org/10.1016/j.autcon.2020.103435.

[11] H. Qin, J.A. Vrugt, X. Xie, Y. Zhou, Improved characterization of underground structure defects from two-stage Bayesian inversion using cross-hole GPR data, Autom. Constr. 95 (2018) 233–244, https://doi.org/10.1016/j.autcon.2018.08.014.

[12] H. Qin, Y. Tang, Z. Wang, X. Xie, D. Zhang, Shield tunnel grouting layer estimation using sliding window probabilistic inversion of GPR data, Tunn. Undergr. Space Technol. 112 (2021), 103913, https://doi.org/10.1016/j.tust.2021.103913.

[13] J. Wang, J. Zhang, A.G. Cohn, Z. Wang, H. Liu, W. Kang, P. Jiang, F. Zhang, K. Chen, W. Guo, Y. Yu, Arbitrarily-oriented tunnel lining defects detection from ground penetrating radar images using deep convolutional neural networks, Autom. Constr. 133 (2022), 104044, https://doi.org/10.1016/j.autcon.2021.104044.

[14] Y. Zhao, J. Wu, X. Xie, J. Chen, S. Ge, Multiple suppression in GPR image for testing back-filled grouting within shield tunnel, in: Proceedings of the 13th International Conference on Ground Penetrating Radar 2010, GPR, 2010, pp. 1–6, https://doi.org/10.1109/ICGPR.2010.5550123.

[15] X. Xie, C. Zeng, Z. Wang, GPR signal enhancement using band-pass and K–L filtering: a case study for the evaluation of grout in a shielded tunnel, J. Geophys. Eng. 10 (2013), 034003, https://doi.org/10.1088/1742-2132/10/3/034003.

[16] J. Zhang, Y. Lu, Z. Yang, X. Zhu, T. Zheng, X. Liu, Y. Tian, W. Li, Recognition of void defects in airport runways using ground-penetrating radar and shallow CNN, Autom. Constr. 138 (2022), 104260, https://doi.org/10.1016/j.autcon.2022.104260.

[17] Y. Zhang, X. Xie, H. Li, B. Zhou, Q. Wang, I. Shahrour, Subway tunnel damage detection based on in-service train dynamic response, variational mode decomposition, convolutional neural networks and long short-term memory, Autom. Constr. 139 (2022), 104293, https://doi.org/10.1016/j.autcon.2022.104293.

[18] H. Qin, D. Zhang, Y. Tang, Y. Wang, Automatic recognition of tunnel lining elements from GPR images using deep convolutional networks with data augmentation, Autom. Constr. 130 (2021), 103830, https://doi.org/10.1016/j.autcon.2021.103830.

[19] H. Liu, C. Lin, J. Cui, L. Fan, X. Xie, B.F. Spencer, Detection and localization of rebar in concrete by deep learning using ground penetrating radar, Autom. Constr. 118 (2020), 103279, https://doi.org/10.1016/j.autcon.2020.103279.

[20] Y. Yue, H. Liu, X. Meng, Y. Li, Y. Du, Generation of high-precision ground penetrating radar images using improved Least Square generative adversarial networks, Remote Sen. (Basel). 13 (2021) 4590, https://doi.org/10.3390/rs13224590.

[21] S. Akcali, F. Erden, Support of Data Augmentation with GAN on Faster R-CNN Based Buried Target Detection, in: 2021 29th Signal Processing and Communications Applications Conference (SIU), IEEE, 2021, pp. 1–4, https://doi.org/10.1109/SIU53274.2021.9477828.

[22] M.-T. Pham, S. Lefevre, Buried Object Detection from B-Scan Ground Penetrating Radar Data Using Faster-RCNN, in: IGARSS 2018–2018 IEEE International Geoscience and Remote Sensing Symposium, IEEE, 2018, pp. 6804–6807, https://doi.org/10.1109/IGARSS.2018.8517683.

[23] S. Lameri, F. Lombardi, P. Bestagini, M. Lualdi, S. Tubaro, Landmine detection from GPR data using convolutional neural networks, in: 2017 25th European Signal Processing Conference (EUSIPCO), IEEE, 2017, pp. 508–512, https://doi.org/10.23919/EUSIPCO.2017.8081259.

[24] T. Yamaguchi, T. Mizutani, T. Nagayama, Mapping subsurface utility pipes by 3-D convolutional neural network and Kirchhoff migration using GPR images, IEEE Trans. Geosci. Remote Sens. 59 (2021) 6525–6536, https://doi.org/10.1109/TGRS.2020.3030079.

[25] J. Feng, L. Yang, E. Hoxha, B. Jiang, J. Xiao, Robotic inspection of underground Utilities for Construction Survey Using a ground penetrating radar, J. Comput. Civ. Eng. 37 (2023) 04022049, https://doi.org/10.1061/(ASCE)CP.1943-5487.0001062.

[26] J. Feng, L. Yang, E. Hoxha, J. Xiao, Improving 3D metric GPR imaging using automated data collection and learning-based processing, IEEE Sensors J. (2022), https://doi.org/10.1109/JSEN.2022.3164707.

[27] T. Chen, C. Guestrin, XGBoost: a scalable tree boosting system, in: Proceedings of the 22nd ACM SIGKDD International Conference on Knowledge Discovery and Data Mining, ACM, New York, NY, USA, 2016, pp. 785–794, https://doi.org/10.1145/2939672.2939785.

[28] A. Shehadeh, O. Alshboul, R.E. al Mamlook, O. Hamedat, Machine learning models for predicting the residual value of heavy construction equipment: an evaluation of modified decision tree, LightGBM, and XGBoost regression, Autom. Constr. 129 (2021), 103827, https://doi.org/10.1016/j.autcon.2021.103827.

[29] C. Warren, A. Giannopoulos, A. Gray, I. Giannakis, A. Patterson, L. Wetter, A. Hamrah, A CUDA-based GPU engine for gprMax: open source FDTD electromagnetic simulation software, Comput. Phys. Commun. 237 (2019) 208–218, https://doi.org/10.1016/j.cpc.2018.11.007.

[30] N.M. Astaf'eva, Wavelet analysis: basic theory and some applications, Physics-Uspekhi. 39 (1996) 1085–1108, https://doi.org/10.1070/PU1996v039n11ABEH000177.

[31] G.R. Lee, R. Gommers, F. Waselewski, K. Wohlfahrt, A. O'leary, PyWavelets: A Python package for wavelet analysis, 2019, https://doi.org/10.21105/joss.01237.

[32] N. Puri, E. Valero, Y. Turkan, F. Bosché, Assessment of compliance of dimensional tolerances in concrete slabs using TLS data and the 2D continuous wavelet transform, Autom. Constr. 94 (2018) 62–72, https://doi.org/10.1016/j.autcon.2018.06.004.

[33] A.F. Oskooi, D. Roundy, M. Ibanescu, P. Bermel, J.D. Joannopoulos, S.G. Johnson, Meep: a flexible free-software package for electromagnetic simulations by the FDTD method, Comput. Phys. Commun. 181 (2010) 687–702, https://doi.org/10.1016/j.cpc.2009.11.008.

[34] I. Laakso, S. Ilvonen, T. Uusitupa, Performance of convolutional PML absorbing boundary conditions in finite-difference time-domain SAR calculations, Phys. Med. Biol. 52 (2007) 7183–7192, https://doi.org/10.1088/0031-9155/52/23/027.

[35] S. Lambot, F. Andre, Full-wave modeling of near-field radar data for planar layered media reconstruction, IEEE Trans. Geosci. Remote Sens. 52 (2014) 2295–2303, https://doi.org/10.1109/TGRS.2013.2259243.

[36] Y. Wan, Z. Zhu, L. Song, S. Song, J. Zhang, X. Gu, X. Xu, Study on temporary filling material of synchronous grouting in the middle of shield, Constr. Build. Mater. 273 (2021), 121681, https://doi.org/10.1016/j.conbuildmat.2020.121681.

[37] S.B. Jones, J.M. Wraith, D. Or, Time domain reflectometry measurement principles and applications, Hydrol. Process. 16 (2002) 141–153, https://doi.org/10.1002/hyp.513.